

## A shear-wave seismic system using full waveform inversion to look ahead of a tunnel-boring machine

Bharadwaj, Pawan; Drijkoningen, Guy; Mulder, Wim; Thorbecke, Jan Willem; Neducza, Borislav; Jenneskens, R

**DOI**

[10.3997/1873-0604.2017014](https://doi.org/10.3997/1873-0604.2017014)

**Publication date**

2017

**Document Version**

Accepted author manuscript

**Published in**

Near Surface Geophysics

**Citation (APA)**

Bharadwaj, P., Drijkoningen, G., Mulder, W., Thorbecke, J. W., Neducza, B., & Jenneskens, R. (2017). A shear-wave seismic system using full waveform inversion to look ahead of a tunnel-boring machine. *Near Surface Geophysics*, 15, 210-224. <https://doi.org/10.3997/1873-0604.2017014>

**Important note**

To cite this publication, please use the final published version (if applicable). Please check the document version above.

**Copyright**

Other than for strictly personal use, it is not permitted to download, forward or distribute the text or part of it, without the consent of the author(s) and/or copyright holder(s), unless the work is under an open content license such as Creative Commons.

**Takedown policy**

Please contact us and provide details if you believe this document breaches copyrights. We will remove access to the work immediately and investigate your claim.

## A shear-wave seismic system using full-waveform inversion to look ahead of a tunnel-boring machine

Pawan Bharadwaj<sup>\*</sup>, Guy Drijkoningen<sup>\*</sup>, Wim Mulder<sup>\*†</sup>,  
Jan Thorbecke<sup>\*</sup>, Borislav Neducza<sup>‡</sup> and Rob Jenneskens<sup>§</sup>

<sup>\*</sup> *Department of Geoscience & Engineering, Delft University of Technology, The Netherlands*

<sup>†</sup> *Shell Global Solutions International BV, Rijswijk, The Netherlands*

<sup>‡</sup> *Geo2X, Oulens-sous-Echallens, Switzerland*

<sup>§</sup> *Seismic Mechatronics BV, Eindhoven, The Netherlands*

### SUMMARY

In the near-surface with unconsolidated soils, shear-wave properties can often be characterized better and with a higher resolution than compressional-wave properties. To enable imaging ahead of a tunnel-boring machine (TBM), we developed a seismic prediction system with a few shear-wave vibrators and horizontal receivers. The boring process is interrupted at regular intervals to carry out active surveys. The vibrators are then pushed against the rock or soil in front of the cutting wheel of the machine. **The design of the vibrators is based on linear synchronous motor technology that can generate very low frequencies, starting at 5 Hz.** These vibrators generate a force in a direction perpendicular to the tunnel axis. Horizontal receivers measure the particle velocity, mainly due to the horizontally polarized shear (SH) waves. Because imaging with conventional migration methods suffers from artefacts, caused by the incomplete aperture and inaccuracies in the assumed velocity model, we use 2-D SH full-waveform inversion (FWI) to resolve the subsurface shear properties. The classic cycle-skipping problem, which can make the application of FWI cumbersome, is avoided by the capacity of the vibrators to

generate low frequencies. In this paper, we demonstrate the capabilities of the proposed seismic system through a number of synthetic and field experiments.

## 1 INTRODUCTION

While excavating a tunnel with a tunnel-boring machine (TBM), the geology and the ground conditions along the planned-tunnel trajectory need to be investigated in order to safely and efficiently carry out underground operations. This entails detecting the occurrence of faults, boulders, foundations, pipes, etc., necessary to avoid hazards that can cause time-consuming delays in the tunnel-boring operations. In order to predict ground conditions ahead of a TBM, seismic exploration techniques such as data acquisition, processing and inversion can be deployed. We will discuss how each of those can be applied to tunnel excavation with a TBM.

Seismic-ground-prediction systems for TBM record waves generated by either controlled sources or its rotating cutter wheel. Hauser (2001) and Petronio & Poletto (2002) obtained interpretable seismic data by cross-correlating signals generated by the cutter wheel with pilot signals recorded at reference receivers. Alternatively, seismic interferometry uses cross-correlation to turn the noise generated by the cutter wheel into useful virtual source records (Poletto & Petronio 2006; Harmankaya *et al.* 2016). However, artefacts are present in the virtual source records since the location of the sources generating the noise is limited to the cutter wheel. Because of this, ground-prediction systems that employ active sources are more successful. In these systems, acquisition is usually carried out with a focus on a particular propagation mode of the seismic waves. The use of Rayleigh waves was proposed by Bohlen *et al.* (2007) and Jetschny (2010), considering a system that excites and records tunnel surface waves at the tunnel wall behind the cutter head of the TBM. With 3-D elastic modelling, they showed that the high-amplitude Rayleigh waves are converted into high-amplitude shear waves at the front face of the tunnel and vice-versa. P waves are commonly used in hydrocarbon exploration. Kneib *et al.* (2000) describes a seismic system for use in soft soil, which uses P waves from 1.8 to 6 kHz. **These are higher compared to the**

10- to 120-Hz frequencies commonly used in surface-seismic techniques. The advantage of using shear or S body waves has been demonstrated by several authors in the case of soft-soil near-surface applications (Omnes 1978; Helbig & Mesdag 1982; Stümpel *et al.* 1984; Guy *et al.* 2003; Haines & Ellefsen 2010). S waves turn out to be very suitable for soft soils since shear waves are not sensitive to the type of fluid or gas in the pores. Hence, estimated shear-wave properties using shear waves correlate well with subsurface lithology. In these soils, propagating shear waves often have a shorter wavelength than P waves (Ghose *et al.* 1998; Haines & Ellefsen 2010; Miller *et al.* 2001), resulting in a better resolution while imaging. Also, in the near surface, where the soft-soil TBM usually operates, relative shear-wave variations are much larger than relative P-wave variations.

Recorded data are processed with the aim to obtain the subsurface parameters that control the seismic wave-propagation. A *reflectivity* image of the subsurface, which depicts the interfaces between different soil types, can be produced by using a subsurface wave-speed or velocity model. The conventional methods of estimating the velocity model directly from seismic data are not fully automatic and require time-consuming human interaction, commonly taking several days to obtain the final images. In tunnel-boring operations, this time is not available: results need to be available within an hour or even minutes, to allow for preventive action when obstacles or potentially dangerous situations ahead of the TBM show up.

Most of the current systems for seismic exploration produce reflectivity images using an assumed velocity model instead of an estimated one. Swinnen *et al.* (2007) discusses an imaging technique based on focusing operators in an assumed model. Tzavaras (2010) applies Kirchhoff pre-stack depth migration and Fresnel-volume migration to produce 3-D reflectivity images in the case of hard-rock tunnelling. Ashida (2001) describes a method to detect the interfaces using data from multi-component receivers. These conventional near-surface imaging techniques all use an assumed velocity model and suffer from various pitfalls (Steeple & Miller 1998). When using shear waves, Miller *et al.* (2001) has shown that Love waves can stack coherently in a common mid-point gather, leading to a wrong interpretation.

Incomplete acquisition, due to the limited space available on the TBM, causes recording footprint noise in conventional images. Inaccuracies in the assumed velocity model will result in migration images that are not properly focused. Therefore, in tunnelling applications, there is a need for a seismic system that can automatically estimate the wave-velocity prior to imaging. Bellino *et al.* (2013) proposes such a fully automatic method, which can estimate the average wave-velocity as well as the distance to an interface.

Recently, an approach called full-waveform inversion (FWI) (Tarantola 1986; Virieux & Operto 2009) has been used to automatically produce a subsurface velocity model for tunnel exploration (Musayev *et al.* 2013; Bharadwaj *et al.* 2015). FWI is a nonlinear data fitting procedure that minimises the misfit between the recorded and the modelled seismic data, in a least-squares sense, to estimate the subsurface parameters. **It requires low frequencies in the data to avoid convergence to local minima caused by the notorious cycle-skipping problem (Virieux & Operto 2009).** The advantage of using FWI over conventional imaging techniques is that the least-squares imaging condition used in FWI will suppress some of the acquisition-related artefacts (Nemeth *et al.* 1999).

The application of waveform inversion to near-surface land data is even more challenging than the marine case because of strong elastic effects such as ground-roll and near-surface attenuation. It is difficult to fit the surface waves due to a heterogeneous near-surface during inversion. In the tunnel environment, the surface waves propagate along the tunnel wall. In order to properly account for the surface waves, elastic modelling is commonly used for near-surface FWI (Bretaudeau *et al.* 2013). Even when using elastic modelling, Brossier *et al.* (2009) illustrated that near-surface FWI generates accurate results via judicious data pre-conditioning and/or muting rather than using surface waves. Moreover, using elastic modelling makes the inverse problem computationally more expensive.

In this paper, we focus on a system that uses horizontally polarised shear (SH) waves (Bharadwaj *et al.* 2015), because shear waves are better suited for exploration in soft soils than P waves, as discussed earlier. Our objective is to investigate and demonstrate the feasibility of using SH waves in unconsolidated soils for TBM-like situations and geometries.

For data acquisition in this system, shear vibrators and receivers are placed on the soil in front of the cutter head to generate and record mainly the SH wavefield. Acquisition is carried out when the tunnel-boring machine (TBM) is not in operation. The design of the vibrator is based on linear synchronous motors technology (Noorlandt *et al.* 2015), which can expand the source frequency band to frequencies as low as 5 Hz. For inverting the data, we use full-waveform inversion to estimate the subsurface shear-wave speed and reflectivity. The capability of the seismic vibrator to generate low frequencies allows us to circumvent the classic problem of cycle-skipping. Of course, this assumes that these frequencies can actually be injected into the subsurface, which may not always be the case. The inability to inject low frequencies is illustrated by an acoustic model with a linear vertical velocity gradient in which waves below a certain frequency do not propagate (Kuvshinov & Mulder 2006).

Since the acquired data need to be processed in near real time with current computing technology, we simplified the SH full-waveform inversion problem to 2D. We applied a crude but simple correction to the measured 3-D data to make them resemble 2-D data. The 2-D approach implicitly assumes invariance in the out-of-plane direction. In that case, the SH waves are decoupled from P, SV, and Rayleigh waves and we can simplify the elastic wave equation to a 2-D SH wave-equation. Due to the absence of Rayleigh waves, the observed data are easier to fit compared to P-wave land datasets. However, Love waves that might be present in the observed data are also modelled by solving the 2-D SH wave equation (Luo *et al.* 2010). It should be noted that Love waves are guided waves that are only generated in the presence of a low S-wave velocity layer close to the sources and receivers. The occurrence of such a layer will be rare as subsurface layering is often nearly horizontal and perpendicular to cutter-head front.

The remainder of the paper is organised into five sections. The next section describes the data acquisition and pre-processing of our system in more detail. After that, we elaborate on the FWI algorithm used to process the data. In the fourth and fifth section, we demon-

strate the application of the seismic system using synthetic scenarios as well as field data, respectively. The last section summarises the paper.

## 2 DATA ACQUISITION AND PRE-PROCESSING

Our system places sources and receivers on the soil along a diameter of the cutter head to generate and record seismic shear waves. Figure 1 shows four possible source-receiver geometries along diameters AA', BB', CC' and DD', respectively. Geometry A is impractical but best illuminates the target. The other geometries use only a few source and receiver positions because of the limited space on a TBM. In the case of a 10-m TBM, geometries B, C and D also take the following practical considerations into account:

- (i) sources and receivers cannot be placed at the same position;
- (ii) sources and receivers cannot be placed within a 1-m radius around the centre of the cutter head;
- (iii) the minimum distance between two positions, each with either a source or receiver, is 0.5 m.

The sources and receivers are pushed against the tunnel face to improve the coupling with the soil. The acquisition takes the rotation and advance of the TBM into account. Making use of the rotation of the TBM, different measurements are combined to obtain data along a particular transect, oriented along one of the diameters of the cutter head. As an example, we can combine the measurements at 45 and 225 degrees to obtain data along the transect BB' in Figure 1. The new dataset will have eight source positions and we refer it as a *combined* dataset. Depending on the rotation speed of the cutter head, combined datasets along 3 to 4 transects can be obtained before the TBM advances ahead, closer to a possible target reflector that needs to be imaged.

In the rest of the paper, we consider pre-processing and inversion for a combined dataset along one particular transect. We choose a coordinate system for this transect such that the  $x$ -axis is always along the transect. The TBM's direction of advance corresponds to

the  $z$ -axis. The vibrator source primarily injects a known sweep as a ground force in the  $y$ -direction, perpendicular to the transect. As a simplified but useful model, we consider 2-D SH waves in the  $[x, z]$ -plane, with the particle velocity in the  $y$ -direction. Shear vibrators and receivers generate and record only the SH wavefield. This is under the assumption that the medium properties should be invariant in the  $y$ -direction. Our vibrator source can excite signals down to 5 Hz, a low enough frequency for shallow shear-wave surveying.

We denote the sweep signal in the frequency domain by  $\Phi_s$ . The uncorrelated recorded data at  $\mathbf{x}_r = [x_r, z_r]$  due to a source at  $\mathbf{x}_s = [x_s, z_s]$  are given in the frequency domain by

$$Q_u(\mathbf{x}_r, f; \mathbf{x}_s) = \Phi_s(f) \Gamma_s^{(0)}(\mathbf{x}_s, f) \Gamma_r^{(0)}(\mathbf{x}_r) I_r(f) G_{3D}(\mathbf{x}_r, f; \mathbf{x}_s). \quad (1)$$

In the above equation,  $\Gamma_s^{(0)}(\mathbf{x}_s, f)$  is a factor that takes frequency-dependent ground coupling at the source position  $\mathbf{x}_s$  into account. Similarly,  $\Gamma_r^{(0)}(\mathbf{x}_r)$  denotes coupling at the receiver position  $\mathbf{x}_r$  and  $I_r(f)$  describes the frequency-dependent instrument response of the receivers used in the survey, which is assumed to be known.  $G_{3D}$  is the 3-D Green's functions or impulse response of the Earth. After acquiring the data, a cross-correlation with the source-sweep signal  $\phi_s$  in the time domain or multiplication with the complex-conjugate spectrum  $\Phi_s^*$  in the frequency domain is performed. Furthermore, to broaden the bandwidth of the data, a spectral division with the amplitude spectrum of the sweep and the amplitude spectrum of the instrument response is carried out. This results in correlated data  $Q^{(3D)}$ , given in the frequency domain by

$$Q^{(3D)}(\mathbf{x}_s, \mathbf{x}_r, f) = \frac{\Phi_s^*(f) \Phi_s(f) \Gamma_s^{(0)}(\mathbf{x}_s, f) \Gamma_r^{(0)}(\mathbf{x}_r) I_r(f) G_{3D}(\mathbf{x}_s, \mathbf{x}_r, f)}{(|\Phi_s(f)|^2 + \epsilon_1)(|I_r(f)| + \epsilon_2)}, \quad (2)$$

where  $\epsilon_1$  and  $\epsilon_2$  are small stabilisation factors.

We invert the combined data along each transect individually as if line sources, which are oriented along the direction perpendicular to the transect, were used. This is a consequence of the 2-D assumption. Since, in reality, we use nearly point-like 3-D sources, we apply an approximate correction to the combined data,  $q^{(3D)}$ , in the time domain to make them resemble 2-D data. We let

$$q^{(2D)}(\mathbf{x}_s, \mathbf{x}_r, t) = \sqrt{t} q^{(3D)}(\mathbf{x}_s, \mathbf{x}_r, t), \quad (3)$$



where the correlated data before and after applying correction are denoted by  $q^{(3D)}$  and  $q^{(2D)}$ , respectively. This correction mainly compensates for the difference in geometrical spreading of the waves (Wapenaar *et al.* 1992); we skipped the customary phase correction by  $\sqrt{if}$ , which is handled instead by including a source-related filter as unknown during the inversion. The correction replaces the 3-D Green's functions  $G_{3D}$  in the equation (2) with the 2-D Green's functions  $G_{2D}$ . After this correction, additional pre-processing such as band-pass filtering, shot-gather normalisation and time-domain tapering, etc., are performed on  $q^{(2D)}$  to obtain the pre-processed observed data  $q_p$ , used for inversion.

Finally, the inversion results from datasets along different transects can be combined into a single 3-D image.

### 3 2-D SH FULL-WAVEFORM INVERSION

An important characteristic of our ground prediction seismic system is its ability to *automatically* produce subsurface maps of the shear-wave velocity,  $c_s$ , and/or mass-density,  $\rho$ . This is mainly achieved by the combination of a specially designed seismic vibrator, based on linear synchronous motors and capable of generating low frequencies, and FWI. Once these maps are produced, the *reflectivity* image of the subsurface can be obtained by taking the derivative of the estimated S-wave impedance in either  $x$ - or  $z$ -direction or by taking the Laplacian. Applying the derivative boosts the reflectors, the interfaces between different materials where seismic waves are reflected.

To compute the modelled data, we solve the 2-D SH wave equation in terms of the particle velocity in the out-of-plane or  $y$ -direction. We use a time-domain staggered-grid finite-difference solver (Virieux 1984) for the forward modelling. To properly account for the effect of the tunnel wall on the wave-propagation, we impose the appropriate Neumann boundary conditions.

Next, we will discuss the objective function to be minimised during full-waveform inversion.

### 3.1 Least-squares Functional With Source Filters and Receiver-coupling Factors

The classic least-squares inversion (Tarantola 1984; Pratt *et al.* 1998; Virieux & Operto 2009; Fichtner 2010; Maurer *et al.* 2012) minimises the difference between the pre-processed observed data and the modelled data iteratively. The objective function with unknown source-related filters and receiver-coupling factors along with the modelled data is given by

$$J_{ls} = \frac{1}{2} \sum_s \sum_r \sum_t [p(\mathbf{x}_r, t; \mathbf{x}_s) *_t \gamma_s(\mathbf{x}_s, t) \gamma_r(\mathbf{x}_r) - q_p(\mathbf{x}_r, t; \mathbf{x}_s)]^2. \quad (4)$$

Here,  $*_t$  denotes convolution in time. We denote the source filters in the time domain and receiver-coupling factors by  $\gamma_s(\mathbf{x}_s, t)$  and  $\gamma_r(\mathbf{x}_r)$ , respectively. Note that the receiver-coupling factors are chosen to be time-independent scalars. The pre-processed observed data and the modelled data are denoted by  $q_p$  and  $p$ , respectively. For further analysis, we consider the data in the frequency domain where convolution in time corresponds to a simple product operation. Using Parseval's theorem, we rewrite the objective function in equation (4) by Fourier transforming the data from time  $t$  to frequency  $f$  as

$$J_{ls} = \frac{1}{4\pi} \sum_s \sum_r \sum_{f \geq 0} |P(\mathbf{x}_r, f; \mathbf{x}_s) \Gamma_s(\mathbf{x}_s, f) \Gamma_r(\mathbf{x}_r) - Q_p(\mathbf{x}_r, f; \mathbf{x}_s)|^2, \quad (5)$$

where we used the fact that  $p$ ,  $q_p$ ,  $\gamma_s$  and  $\gamma_r$  are real valued. Here,  $P$ ,  $Q_p$ ,  $\Gamma_s$  and  $\Gamma_r$  denote the frequency domain representations of  $p$ ,  $q_p$ ,  $\gamma_s$  and  $\gamma_r$ , respectively. Note that  $\Gamma_r = \gamma_r$ , as the receiver-coupling factors are frequency independent.

During the inversion,  $\Gamma_s$  and  $\Gamma_r$  are to be estimated in addition to the medium parameters. The source filters and the receiver-coupling factors compensate for additional unknowns such as source signature and ground coupling at source and receiver locations in the seismic experiment. In order to understand their significance, we consider a case in which the modelled data are generated for the correct medium parameters with a source wavelet  $\Phi$ . For

that case, we express the pre-processed observed data discussed in the previous section as

$$Q_p(\mathbf{x}_s, \mathbf{x}_r, f) \approx \frac{\Phi_s^*(f) \Phi_s(f) \Gamma_s^{(0)}(\mathbf{x}_s, f) \Gamma_r^{(0)}(\mathbf{x}_r) I_r(f) G_{2D}(\mathbf{x}_s, \mathbf{x}_r, f)}{(|\Phi_s|^2 + \epsilon_1)(|I_r| + \epsilon_2)}, \quad (6)$$

$$\approx \underbrace{\frac{\Phi_s^*(f) \Phi_s(f) \Gamma_s^{(0)}(\mathbf{x}_s, f) I_r(f)}{\Phi(f)(|\Phi_s|^2 + \epsilon_1)(|I_r| + \epsilon_2)}}_{\Gamma_s(\mathbf{x}_s, f)} \underbrace{\Gamma_r^{(0)}(\mathbf{x}_r)}_{\Gamma_r(\mathbf{x}_r)} P(\mathbf{x}_s, \mathbf{x}_r, f). \quad (7)$$

It is obvious from the above equation that the factors  $\Gamma_s$  and  $\Gamma_r$  are required to match the modelled data to the observed data even when the correct medium parameters are used.

We use gradient-based techniques to minimise the functional  $J_{ls}$ . Hence, we first derive the expressions for the gradient of  $J_{ls}$  with respect to the modelled data, source filters and receiver-coupling factors. These are denoted by  $\nabla_p J_{ls}$ ,  $\nabla_{\gamma_s} J_{ls}$  and  $\nabla_{\gamma_r} J_{ls}$ , respectively. Then, we will explain our optimisation strategy.

### 3.1.1 Gradient With Respect To Medium Parameters

The gradient of  $J_{ls}$  with respect to the medium parameters,  $c_s$  and  $\rho$ , is required to update the subsurface maps. It is computed by correlating the forward-propagated source wavefield with the adjoint wavefield at each point in the subsurface. The adjoint wavefield is generated by injecting the adjoint source functions  $\nabla_p J_{ls}$  from the receiver positions. In order to compute the adjoint source functions for the least-squares functional with source filters and receiver-coupling factors, the following steps are performed sequentially:

- (i) source filters and receiver-coupling factors are applied to the modelled data,
- (ii) the difference between the data after applying filters and the observed data is calculated,
- (iii) the difference is cross-correlated with the source filters and multiplied with receiver-coupling factors.

In order to derive an expression for  $\nabla_P J_{ls}$ , we rewrite equation (5) using the real and imaginary parts of the absolute-valued data as

$$J_{ls} = \frac{1}{4\pi} \sum_s \sum_r \sum_{f \geq 0} \{ [\text{Re}(P) \text{Re}(\Gamma_s) \Gamma_r - \text{Im}(P) \text{Im}(\Gamma_s) \Gamma_r - \text{Re}(Q_p)]^2 + [\text{Im}(P) \text{Re}(\Gamma_s) \Gamma_r + \text{Im}(\Gamma_s) \text{Re}(P) \Gamma_r - \text{Im}(Q_p)]^2 \}. \quad (8)$$

We now differentiate the above equation with respect to the real and imaginary parts of the modelled data  $P$  to obtain

$$\begin{aligned} \nabla_P J_{ls} &= \nabla_{\text{Re}(P)} J_{ls} + i \nabla_{\text{Im}(P)} J_{ls}, \\ &= \frac{1}{2\pi} [P(\mathbf{x}_r, f; \mathbf{x}_s) \Gamma_s(\mathbf{x}_s, f) \Gamma_r(\mathbf{x}_r) - Q_p(\mathbf{x}_r, f; \mathbf{x}_s)] \Gamma_s^*(\mathbf{x}_s, f) \Gamma_r(\mathbf{x}_r), \end{aligned} \quad (9)$$

where the superscript  $*$  denotes complex conjugation. Alternatively, the Wirtinger calculus can be used to derive an expression for  $\nabla_P J_{ls}$ .

Using the chain rule, we can write the derivative of the functional with respect to the modelled data in the time domain as

$$\nabla_P J_{ls} = [p(\mathbf{x}_r, t; \mathbf{x}_s) *_t \gamma_s(\mathbf{x}_s, t) \gamma_r(\mathbf{x}_r) - q_p(\mathbf{x}_r, t; \mathbf{x}_s)] \otimes_t \gamma_s(\mathbf{x}_s, t) \gamma_r(\mathbf{x}_r), \quad (10)$$

where  $\otimes_t$  denote cross-correlation.

### 3.1.2 Updating Source and Receiver Filters

In order to compute the gradient of the objective function in the equation (8) with respect to the source filters, the same steps as those for the gradient in the preceding subsection are followed except for the step (iii), where the difference is cross-correlated with the modelled data and multiplied with the receiver-coupling factors. Now, an additional summation over the receiver coordinate is also performed. This leads to

$$\nabla_{\gamma_s} J_{ls} = \sum_r [p(\mathbf{x}_r, t; \mathbf{x}_s) *_t \gamma_s(\mathbf{x}_s, t) \gamma_r(\mathbf{x}_r) - q_p(\mathbf{x}_r, t; \mathbf{x}_s)] \otimes_t p(\mathbf{x}_r, t; \mathbf{x}_s) \gamma_r(\mathbf{x}_r), \quad (11)$$

Similarly, the gradient with respect to the receiver-coupling factors can be computed as

$$\nabla_{\gamma_r} J_{ls} = \sum_s \sum_t [p(\mathbf{x}_r, t; \mathbf{x}_s) *_t \gamma_s(\mathbf{x}_s, t) \gamma_r(\mathbf{x}_r) - q_p(\mathbf{x}_r, t; \mathbf{x}_s)] \otimes_t p(\mathbf{x}_r, t; \mathbf{x}_s) \otimes_t \gamma_s(\mathbf{x}_s, t). \quad (12)$$

### 3.2 Optimisation Strategy

We estimate the unknown medium parameters, source filters and receiver-coupling factors that affect equation (4) by using an optimisation strategy outlined by the flowchart of Figure 2. We use the conjugate-gradient minimisation scheme that uses the gradients of the objective function with respect to the unknowns. The inputs of the optimisation strategy are the pre-processed observed data, the initial values of the source filters, the receiver-coupling factors and the medium parameters. Initially, we choose the receiver-coupling factors to be equal for all the receivers, for instance  $\gamma_r = 1$ , and the source filters all zero. The initial shear-wave velocity model is a homogeneous one and the velocity is chosen based on the move-out of the direct arrivals in the observed data.

The outermost loop in our strategy runs over the frequency band ( $i_b$ ) of the observed data selected for inversion. This approach corresponds to multi-scale full-waveform inversion (Bunks *et al.* 1995; Boonyasiriwat *et al.* 2009), where we first invert the low-frequency data and then gradually include higher frequencies. The innermost loop consists of two round-trips ( $i_r$ ) for the observed data in a given frequency band. The output of the first round trip is used as input to the second. In each round-trip, the unknowns that should minimize  $J_{ls}$  are estimated in the following order:

- (i) source-related filters,  $\gamma_s$ , having both positive and negative lags, where a maximum lag time is chosen to prevent error-leakage from medium parameters;
- (ii) receiver-coupling factors,  $\gamma_r$ , which should be positive;
- (iii) the velocity,  $c_s$ , everywhere ahead of the TBM, by fitting both the direct arrivals and the reflections in the observed data;
- (iv) the velocity,  $c_s$ , in a region with roughly one dominant wavelength away from the TBM, so that the minimization mainly fits the arrivals reflected off the scatterers in the region. This is accomplished by muting the gradient close to the TBM.

While updating one of the unknowns, the other unknowns are kept constant. During the step (iv), we focus on fitting only the reflections in the data because the direct arrivals are

often stronger and dominate the inversion during step (iii). Note that the limited maximum offset causes refractions and diving waves to be absent. The motivation behind performing more than one round trip is that the estimate of the source and receiver filters is improved during the second round-trip when an updated velocity model from the first round-trip is available, assuming that each step reduces the error between modelled and observed data. Similarly, the velocity model is better estimated in the second round-trip since improved filters are applied to the modelled data.

#### 4 SYNTHETIC SCENARIOS

In order to evaluate the performance of 2-D SH FWI in a TBM-like setting, we present results from **three typical hazardous scenarios from the tunnelling industry**. Table 1 lists the values for the seismic shear-wave properties of various subsurface materials, used to generate 2-D synthetic  $c_s$  and  $\rho$  models. Random velocity and density perturbations (approximately 10% of the background) are added to the synthetic models to make them more realistic. For each scenario, synthetic models serve as input to the 2-D SH finite-difference wave-equation solver to generate synthetic ‘observed’ data. Table 2 lists the parameters chosen for the forward modelling. The records corresponding to each receiver are then multiplied with a random number between 0.2 to 1 to introduce receiver-coupling factors  $\Gamma_r^{(0)}(\mathbf{x}_r)$ , as in Equation (1). As specified in Table 2, we deliberately chose different source wavelets for the observed data and for the initially modelled data so that the estimation of the source filter is necessary during the inversion.

We invert only for the shear-wave speed,  $c_s$ , while the source filter is assumed to be independent of the source location. Table 3 summarizes the inversion parameters. The mass-density,  $\rho$ , is taken as a constant during the inversion. The tunnel axis is assumed to be at a depth of 10m below the surface at  $z = 0$ . The sources and receivers are constrained to depths between 5 m to 15 m below the surface, thereby assuming a TBM diameter of 10 m (see, e.g., Figure 1). Absorbing boundary conditions are applied at the surface. **For quantitative evaluation of the output model vectors, say  $\mathbf{m}$ , we used a correlation measure**

with respect to a reference model vector,  $\mathbf{m}_0$ , given by

$$C_{\mathbf{m},\mathbf{m}_0} = \frac{\langle \mathbf{m}, \mathbf{m}_0 \rangle}{\langle \mathbf{m}_0, \mathbf{m}_0 \rangle}, \quad (13)$$

where  $\langle \cdot, \cdot \rangle$  denotes zero-lag correlation.

#### 4.1 Scenario A: Abrupt Change

This scenario defines a sudden change in geology, for instance, when a compacted sand layer lies next to clay. Figures 3e and 3j show 2-D cross-sections of the shear-wave velocity and mass-density models for such a scenario. Here, the sources and receivers are positioned in the sand and we consider all the four acquisition geometries shown in Figure 1. As listed in Table 2, we used a 40–80–300–400 Hz Ormsby source wavelet, plotted in Figure 4, to generate the observed seismic data. To generate the modelled data, we used a 40–400 Hz fourth-order minimum-phase Butterworth wavelet. Maximum recording time for the observed and the modelled data is 0.1 s.

The source filter,  $\gamma_s$ , has both positive and negative lags with a maximum lag time of 0.01 s. We applied multi-scale full-waveform inversion by first inverting the data between 40–70 Hz, followed by three bands: 40–100 Hz, 40–200 Hz, and 40–400 Hz, as shown in the Table 3. We start the inversion from a homogeneous velocity model with  $c_s = 400$  m/s. As already mentioned, the mass-density is kept constant during the inversion.

The updated velocity models after inversion with the acquisition geometries A, B, C and D are displayed in Figures 3a–d. The cross-hatched pattern indicates the location of the TBM. The horizontal and vertical reflectivity models, shown in Figures 3f–i and Figures 3k–n, are obtained by differentiating the output velocity models with respect to  $x$  and  $z$ , respectively. The abrupt change in geology is well imaged with acquisition geometries A and B, although better with A than with B. This is caused by the fact that more sources and receivers are used in acquisition geometry A. In both cases, the horizontal reflectivity models depict a reflector that is positioned correctly. In addition to the first reflector, the inversion has also imaged a ghost reflector that can be misinterpreted as a second reflector. Acquisition geometries C and D were unsuccessful in illuminating the target reflector, particularly

in the centre, because they use a smaller number of sources. As shown in the Figure 3, the correlation measure (Equation 13) decreases (by a factor of 2) for these geometries compared to geometry B, where the outputs using geometry A are chosen as reference. This indicates that one should aim for an acquisition with properly distributed sources and receivers. In all cases, the estimated source filters and receiver-coupling factors after inversion are close to their true values. In the case of geometry B, the source wavelet used to generate the observed data and the estimated source filter  $\gamma_s$  applied to the modelled-data wavelet  $\phi$  are plotted in Figure 4. Figure 5 shows the estimated and true receiver-coupling factors.

#### 4.1.1 Advance of the TBM

As the TBM advances, it approaches the subsurface target that we would like to image. Our system performs inversion at each stage of advance separately. Often the target is better illuminated when the TBM comes closer, resulting in a better image. To demonstrate this fact, we consider the current scenario with three stages of advance and with acquisition geometry B. During the first stage, the TBM is far away from the target reflector as in Figure 6a. The position of the target reflector cannot be determined accurately because of the lack of offset-dependent information, which determines the background velocity. The image of the target reflector in the output reflectivity model of Figures 6d appears closer to the TBM than in the actual synthetic model in Figure 6g. It can be noticed that, in the output velocity model (Figure 6a), the velocity between the reflector and the TBM is lower than the actual value. The inversion results from the second stage, Figures 6b and 6e, show that the target is better illuminated and slightly better positioned. In the third stage, the inversion results in Figures 6c and 6f show that the target is correctly imaged.

In practice, it is possible to use the inversion outputs from a particular stage as initial models for the next stage. Also, the datasets from two or three consecutive stages can be combined to perform joint inversion.



#### 4.2 Scenario B: Hard-rock Inclusion

In this scenario, we used the  $c_s$  and  $\rho$  models shown in Figures 7e and 7j. The models represent a rock-type inclusion in a soft-soil environment. Often, this type of inclusion is more or less horizontal in young sediments. We use clay as the background medium and limestone for the hard inclusion. The shear-wave velocity of the propagating waves in clay is lower than in sand or limestone and high frequencies are attenuated due to losses. Based on our experience with field experiments, we used a 40-Hz Ricker wavelet to generate the observed seismic data. The modelling and inversion parameters for this scenario are summarized in Tables 2 and 3, respectively. In this example, we invert the observed data only in a single frequency band because the initial homogeneous velocity model has roughly the same background velocity as the actual model. The output velocity models, horizontal-reflectivity models and vertical-reflectivity models after inversion using different acquisition geometries are plotted in Figure 7. **The correlation measure is only slightly lower for geometries C and D compared to geometry B, where the outputs using geometry A are chosen as reference.**

In all cases, we were able to image only the tip of the inclusion in front of the TBM. This was to be expected since the source cannot illuminate the sides of the inclusion, in a way that would cause waves to be reflected back to the receivers. All the acquisition geometries image the tip of the inclusion well. However, it can be seen that using less source positions, as in the case of geometries C and D, causes more artefacts in the output velocity models.

#### 4.3 Scenario C: Fault Region

Figures 8e and 8j show the velocity and density models corresponding to this scenario. The aim is to predict the characteristics of the fault region, in particular its width and filling material. We consider the case where the geology is the same on both sides of the fault region. The medium inside the fault region is considered to be clay and the background medium is considered to be sand. Since the sources and receivers are in the sand area, we used the same modelling and inversion parameters (Tables 2 and 3) as those for the abrupt-change scenario. The output velocity models, horizontal-reflectivity models and vertical-reflectivity

models after inversion with the different acquisition geometries are displayed in Figure 8. The fault region model is only imaged properly in the case of geometries A and B. Again, when compared to geometry B, the correlation measure is lower by almost a factor two when using geometries C and D, because of the smaller number of sources and receivers. The width of the reconstructed fault structure exceeds the actual width. The exact velocity of the filling material, clay, cannot be determined by the inversion because of the limited aperture. However, the horizontal-reflectivity images depict the boundaries of the fault region. Note that the imaged reflector corresponding to the outer boundary of the fault region might also be misinterpreted as a ghost reflector in Figure 3.

## 5 FIELD TEST: INCLUSION

So far, we have considered synthetic scenarios. We will continue with a scenario that was built in the field. This took place at a site near Eindhoven Airport in the Netherlands, where a number of scenarios were built. Here, we will discuss only one of them, namely an inclusion. A TBM setting was simulated by having a fixed spread at the surface as if that spread would represent the source(s) and receivers on the cutter head of a TBM. Therefore, this mimicks a TBM measuring in the vertical rather than the horizontal direction, as considered in the preceding section. The rotation of the cutter head was simulated by rotating the spread by an angle of 60 degrees compared to the previous one, keeping the central point of the spread fixed.

In order to simulate an inclusion, a vertical concrete tube of 1.2 m height and 0.6 m diameter was filled with gravel and placed at a depth of 6 m, exactly below the middle point of the spread. The tube was buried underneath a thick cover of clay. The clay cover was subsequently peeled off, mimicking the advancement of the TBM. Here we will show the results after removing 2 m of the clay cover, when the concrete tube was 4 m, below the acquisition surface; in Figures 10 and 11, the tube is situated at  $z = 6$  m, while the acquisition surface was at  $z = 2$  m.

As for the receivers: the experiment was conducted with seventeen 10-Hz horizontal

SM9<sup>©</sup> geophones from the company ION, evenly spaced at 0.5 m from  $x = -4$  m to 4 m, mimicking the case of a TBM with a diameter of 8 m. And for the type of seismograph: we used a 24-bit Sigma Delta system Geode<sup>©</sup> from the company Geometrics. The geophones measure the out-of-plane component of the particle velocity, in this case the SH waves. As for the source, we generated an out-of-plane component of the force, i.e., generating SH waves. The shear-wave vibrator was placed at the positions of the 1st, 3rd, 5th, 13th, 15th and 17th receivers, so at  $x = -4$  m,  $-3$  m,  $-2$  m,  $2$  m,  $3$  m, and  $4$  m. With the source placed there, the geophone was removed from that particular position and put back when the source was moved to the next position. Figure 9, taken during the acquisition, shows a picture of the whole set up.

We used the newly developed shear-wave vibrator that allowed us to input a broadband signal into the ground, namely a linear sweep from 5 to 120 Hz, including the low frequencies required by FWI to perform the processing in a fully automated way.

Observed shot gathers for a source at  $x = 4$  m after pre-processing are plotted in Figures 10a and 11a. The pre-processing consisted in applying the correlation with the input sweep, the correction for the amplitude of the receiver’s transfer function and the correction for 3D-to-2D amplitudes, all according to Equation (3). We fitted the recorded shot gathers starting from a homogeneous Earth model with  $c_s = 110$  m/s and  $\rho = 1$  g/cm<sup>3</sup>. The mass-density model is not updated during the inversion and only the data in the bandwidth 50–120 Hz are used. Unfortunately, frequencies below 50 Hz had to be muted to suppress the noise from nearby vehicles. We noticed that such a muting operation did not cause severe cycle-skipping problems in this test.

We use the optimisation strategy shown in Figure 2. After inversion, the modelled data, plotted in Figures 10b and 11b, match the observed data quite well. Figures 10c and 11c show the final output velocity model for both transects. Figures 10d and 11d depict the vertical derivatives of the output velocity models. Note that in Figure 11d, there is a slight mismatch with the true position of the buried target. In Figure 11b, there is a data mismatch around an offset of 4 to 5 m. For each transect, the inversion of pre-processed data takes about half

an hour on six compute cores. The results were used for interpretation and we were able to detect a high-velocity anomaly, corresponding to the location of the concrete-tube inclusion. This demonstrates the success of our SH-wave seismic system to produce subsurface images, including the possibility to have a fully automatic system.

## 6 DISCUSSION AND CONCLUSIONS

During the field experiment, the recorded signals below 50 Hz are masked by the noise due to nearby vehicles. In these situations with unreliable low frequencies in the data, the inversion is prone to suffer from the cycle-skipping problem (Mulder & Plessix 2008). The cycle-skipping problem is severe only when recovering low-wavenumber anomalies, which is not the case in our field example. Alternative inversion algorithms are proposed by many authors (van Leeuwen & Mulder 2010; Bozdağ *et al.* 2011; Bharadwaj *et al.* 2016; Li & Demanet 2016) to reduce the severity of this problem.

In the examples of this paper, we only estimated the subsurface shear-wave velocity. In addition to that, full-waveform inversion can also estimate the mass-density of the subsurface provided if the inverse problem is properly regularized with necessary constraints.

We developed a ground prediction system that uses horizontally polarised shear-waves for imaging in front of a TBM, in the case of unconsolidated soils. **Compared to the conventional systems, this system produces subsurface images with less artefacts, in an automated way.** Seismic data are acquired by the receivers on the cutter head of the TBM, which also hosts the vibrators. The design of the vibrator is based on linear synchronous motors technology that is capable of generating low frequencies. With these low frequencies, the seismic system can use full-waveform inversion as an imaging engine and estimate the shear-wave velocity model required for subsurface imaging in a fully automatic way, without human intervention. In addition to shear-wave velocity, our full-waveform inversion algorithm estimates the source-related filters and the receiver-coupling factors.

We investigated the potential of the seismic system using both synthetic and field experiments with TBM configurations. The synthetic examples use different acquisition geometries

that take practical constraints into account. We showed that the output subsurface image quality goes up almost by a factor of two when an acquisition with properly distributed sources and receivers is used. In the case of the field experiments, the system was able to detect a buried object in the subsurface. Hence, our ground prediction system can be used for hazard assessment during TBM operation in soft soils.

## 7 ACKNOWLEDGEMENTS

This work is a part of the NeTTUN project, funded from the European Commissions Seventh Framework Programme for Research, Technological Development and Demonstration (FP7 2007-2013) under Grant Agreement 280712. This work was sponsored by NWO Exacte Wetenschappen (Physical Sciences) for the use of supercomputer facilities, with financial support from the Nederlandse Organisatie voor Wetenschappelijk Onderzoek (Netherlands Organisation for Scientific Research, NWO). Part of the computations were carried out on the Dutch national e-infrastructure with the support of the SURF Foundation ([www.surfsara.nl](http://www.surfsara.nl)).

## REFERENCES

- Ashida, Yuzuru, 2001. Seismic imaging ahead of a tunnel face with three-component geophones, *International Journal of Rock Mechanics and Mining Sciences*, **38**(6), 823–831.
- Bellino, Andrea, Garibaldi, Luigi, & Godio, Alberto, 2013. An automatic method for data processing of seismic data in tunneling, *Journal of Applied Geophysics*, **98**, 243–253.
- Bharadwaj, P, Mulder, WA, Drijkoningen, GG, & Reijnen, R, 2015. Looking ahead of a tunnel boring machine with 2-D SH full waveform inversion, in *77th EAGE Conference and Exhibition 2015*.
- Bharadwaj, Pawan, Mulder, Wim, & Drijkoningen, Guy, 2016. Full waveform inversion with an auxiliary bump functional, *Geophysical Journal International*, **206**(2), 1076–1092.
- Bohlen, Thomas, Lorang, Ulrich, Rabbel, Wolfgang, Müller, Christof, Giese, Rüdiger, Lüth, Stefan, & Jetschny, Stefan, 2007. Rayleigh-to-shear wave conversion at the tunnel face: From 3D-FD modeling to ahead-of-drill exploration, *Geophysics*, **72**(6), T67–T79.
- Boonyasiriwat, Chaiwoot, Valasek, Paul, Routh, Partha, Cao, Weiping, Schuster, Gerard T, & Macy, Brian, 2009. An efficient multiscale method for time-domain waveform tomography, *Geophysics*, **74**(6), WCC59–WCC68.
- Bozdağ, Ebru, Trampert, Jeannot, & Tromp, Jeroen, 2011. Misfit functions for full waveform inversion based on instantaneous phase and envelope measurements, *Geophysical Journal International*, **185**(2), 845–870.
- Brethoudeau, François, Brossier, Romain, Leparoux, Donatienne, Abraham, Odile, & Virieux, Jean, 2013. 2D elastic full-waveform imaging of the near-surface: Application to synthetic and physical modelling data sets, *Near Surface Geophysics*, **11**(3), 307–316.
- Brossier, Romain, Operto, Stéphane, & Virieux, Jean, 2009. Seismic imaging of complex onshore structures by 2D elastic frequency-domain full-waveform inversion, *Geophysics*, **74**(6), WCC105–WCC118.
- Bunks, Carey, Saleck, Fatimetou M, Zaleski, S, & Chavent, G, 1995. Multiscale seismic waveform inversion, *Geophysics*, **60**(5), 1457–1473.
- Fichtner, Andreas, 2010. *Full seismic waveform modelling and inversion*, Springer.
- Ghose, Ranajit, Nijhof, Vincent, Brouwer, Jan, Matsubara, Yoshikazu, Kaida, Yasuhiro, & Takahashi, Toru, 1998. Shallow to very shallow, high-resolution reflection seismic using a portable vibrator system, *Geophysics*, **63**(4), 1295–1309.
- Guy, Erich D, Nolen-Hoeksema, Richard C, Daniels, Jeffrey J, & Lefchik, Thomas, 2003. High-resolution SH-wave seismic reflection investigations near a coal mine-related roadway collapse feature, *Journal of Applied Geophysics*, **54**(1), 51–70.
- Haines, Seth S & Ellefsen, Karl J, 2010. Shear-wave seismic reflection studies of unconsolidated

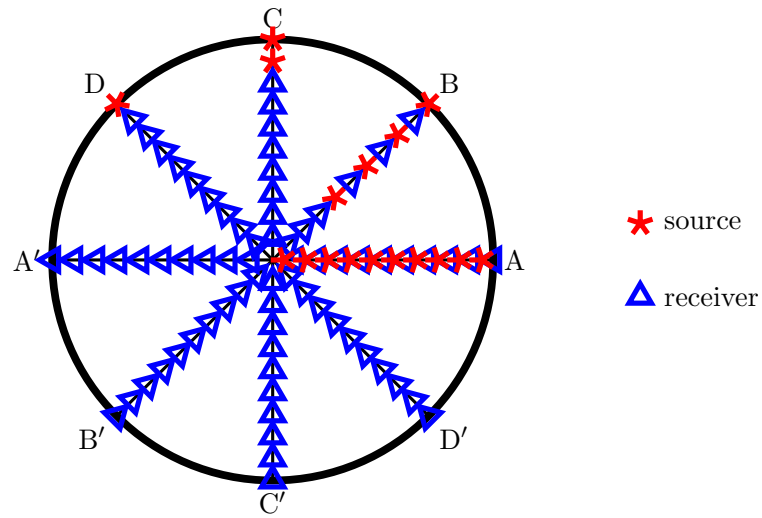
- sediments in the near surface, *Geophysics*, **75**(2), B59–B66.
- Harmankaya, U, Kaslilar, A, Wapenaar, K, & Draganov, D, 2016. Locating scatterers ahead of a tunnel boring machine using noise correlation, in *78th EAGE Conference and Exhibition 2016*.
- Hauser, Ernest C, 2001. Detection and location of obstructions ahead of a tunnel boring machine using the tunneling vibrations as a seismic source: The first successful example, in *2001 Symposium on Application of Geophysics to Environmental and Engineering Problems (SAGEEP)*.
- Helbig, K & Mesdag, CS, 1982. The potential of shear-wave observations, *Geophysical Prospecting*, **30**(4), 413–431.
- Jetschny, Stefan, 2010. *Seismic prediction and imaging of geological structures ahead of a tunnel using surface waves*, Ph.D. thesis, Karlsruhe Inst. für Technologie, 2010.
- Kneib, Guido, Kassel, Andreas, & Lorenz, Klaus, 2000. Automatic seismic prediction ahead of the tunnel boring machine, *First Break*, **18**(7).
- Kuvshinov, Boris N & Mulder, Wim A, 2006. The exact solution of the time-harmonic wave equation for a linear velocity profile, *Geophysical Journal International*, **167**(2), 659–662.
- Li, Yunyue Elita & Demanet, Laurent, 2016. Full-waveform inversion with extrapolated low-frequency data, *Geophysics*, **81**(6), R339–R348.
- Luo, Yinhe, Xia, Jianghai, Xu, Yixian, Zeng, Chong, & Liu, Jiangping, 2010. Finite-Difference Modeling and Dispersion Analysis of High-Frequency Love Waves for Near-Surface Applications, *Pure and Applied Geophysics*, **167**(12), 1525–1536.
- Maurer, Hansruedi, Greenhalgh, Stewart A, Manukyan, Edgar, Marelli, Stefano, & Green, Alan G, 2012. Receiver-coupling effects in seismic waveform inversions, *Geophysics*, **77**(1), R57–R63.
- Miller, Richard D, Xia, Jianghai, & Park, Choon B, 2001. Love waves: A menace to shallow shear wave reflection surveying, in *71st Annual Meeting Society of Exploration Geophysicists Expanded Abstracts*, pp. 1377–1380.
- Mulder, WA & Plessix, R-E, 2008. Exploring some issues in acoustic full waveform inversion, *Geophysical Prospecting*, **56**(6), 827–841.
- Musayev, Khayal, Hackl, Klaus, & Baitsch, Matthias, 2013. Frequency domain waveform inversion in a tunnel environment, *Proceedings of Applied Mathematics and Mechanics*, **13**(1), 323–324.
- Nemeth, Tamas, Wu, Chengjun, & Schuster, Gerard T, 1999. Least-squares migration of incomplete reflection data, *Geophysics*, **64**(1), 208–221.
- Noorlandt, Rik, Drijkoningen, Guy, Dams, Johan, & Jenneskens, Rob, 2015. A seismic vertical vibrator driven by linear synchronous motors, *Geophysics*, **80**(2), EN57–EN67.
- Omnes, Gildas, 1978. Exploring with SH-waves, *Canadian Journal of Exploration Geophysics*, **14**, 40–49.
- Petronio, Lorenzo & Poletto, Flavio, 2002. Seismic-while-drilling by using tunnel boring machine

- noise, *Geophysics*, **67**(6), 1798–1809.
- Poletto, Flavio & Petronio, Lorenzo, 2006. Seismic interferometry with a TBM source of transmitted and reflected waves, *Geophysics*, **71**(4), SI85–SI93.
- Pratt, R. G., C.Shin, & Hicks, G.J., 1998. Gauss-Newton and full Newton methods in frequency-space seismic waveform inversion, *Geophysical Journal International*, **133**(2), 341–362.
- Steeple, Don W & Miller, Richard D, 1998. Avoiding pitfalls in shallow seismic reflection surveys, *Geophysics*, **63**(4), 1213–1224.
- Stümpel, H, Kähler, S, Meissner, R, & Milkereit, B, 1984. The use of seismic shear waves and compressional waves for lithological problems of shallow sediments, *Geophysical Prospecting*, **32**(4), 662–675.
- Swinnen, G, Thorbecke, JW, & Drijkoningen, GG, 2007. Seismic imaging from a TBM, *Rock Mechanics and Rock Engineering*, **40**(6), 577–590.
- Tarantola, A., 1984. Inversion of seismic reflection data in the acoustic approximation, *Geophysics*, **49**(8), 1259–1266.
- Tarantola, A., 1986. strategy for nonlinear elastic inversion of seismic reflection data, *Geophysics*, **51**, 1893–1903.
- Tzavaras, Johannes, 2010. *3D Tunnel Seismic Imaging*, Ph.D. thesis, Freie Universität Berlin.
- van Leeuwen, T & Mulder, W. A., 2010. A correlation-based misfit criterion for wave-equation travelttime tomography, *Geophysical Journal International*, **182**(3), 1383–1394.
- Virieux, Jean, 1984. SH-wave propagation in heterogeneous media: velocity-stress finite-difference method, *Geophysics*, **49**(11), 1933–1942.
- Virieux, J. & Operto, S., 2009. An overview of full-waveform inversion in exploration geophysics, *Geophysics*, **74**(6), WCC1–WCC26.
- Wapenaar, CPA, Verschuur, Dirk J, & Herrmann, Philippe, 1992. Amplitude preprocessing of single and multicomponent seismic data, *Geophysics*, **57**(9), 1178–1188.



**LIST OF FIGURES**

- 1 Cutter head of the tunnel-boring machine showing source-receiver acquisition geometries along different diameters.
- 2 Flowchart depicting the optimisation strategy used to estimate source, receivers filters and shear-wave velocity in the medium. The subscript  $b$  in  $i_b$  stands for frequency band and the subscript  $r$  in  $i_r$  stands for round-trip.  $N_b$  denotes the total number of frequency bands inverted.
- 3 Scenario A: Abrupt Change. The output  $c_s$  models using geometries A, B, C and D are plotted in (a), (b), (c) and (d), respectively. The corresponding horizontal and vertical derivatives of the  $c_s$  models are plotted in (f)–(i) and (k)–(n), respectively. The  $c_s$  (e) and  $\rho$  (j) models used to generate the observed data are shown as well. Crosshatch pattern indicates the location of the TBM. **The correlation measures of the outputs using geometries B, C and D are also given, where the outputs using geometry A are chosen for reference.**
- 4 For the abrupt-change scenario, the source wavelet used to generate the synthetic *observed* data is plotted in black. The estimated source filter  $\gamma_s$  applied to the modelled-data wavelet  $\phi$  is plotted in red, when using acquisition geometry B.
- 5 For the abrupt-change scenario, the true and estimated receiver-coupling factors are plotted in black and red, respectively. Acquisition geometry B is used.
  
- 6 Inversion results during three stages of advance of the TBM for Scenario A using acquisition geometry B. The output velocity models from inversion are plotted in (a)–(c). The horizontal derivatives of the output velocity models are plotted in (d)–(f), which depict the target reflector. The cross-hatched pattern indicates the location of the TBM. The  $c_s$  (g) and  $\rho$  (h) models used to generate the observed data are also plotted.
- 7 Same as Figure 3, except for Scenario B: Hard-rock Inclusion.
- 8 Same as Figure 3, except for Scenario C: Fault Region.
- 9 Field acquisition with the shear-wave vibrator (marked by the red box), especially designed for this application, and the receivers (blue box) along a transect (dashed line) similar to what is typical for a TBM situation.
- 10 The pre-processed data and inversion results of the first transect. a) Observed shot gather for a source at  $x = 4$  m. b) Modelled shot gather after inversion. c) Estimated shear-wave velocity model of subsurface. d) Image of subsurface depicting the inclusion. The actual location of the inclusion is marked by the red box.
- 11 Same as Figure 10, except for the data corresponding to the second transect.



Geometry	Number of Sources	Number of Receivers	Practical?
A	20	20	no
B	4	16	yes
C	2	18	yes
D	1	19	yes

**Figure 1.** Cutter head of the tunnel-boring machine showing source-receiver acquisition geometries along different diameters.

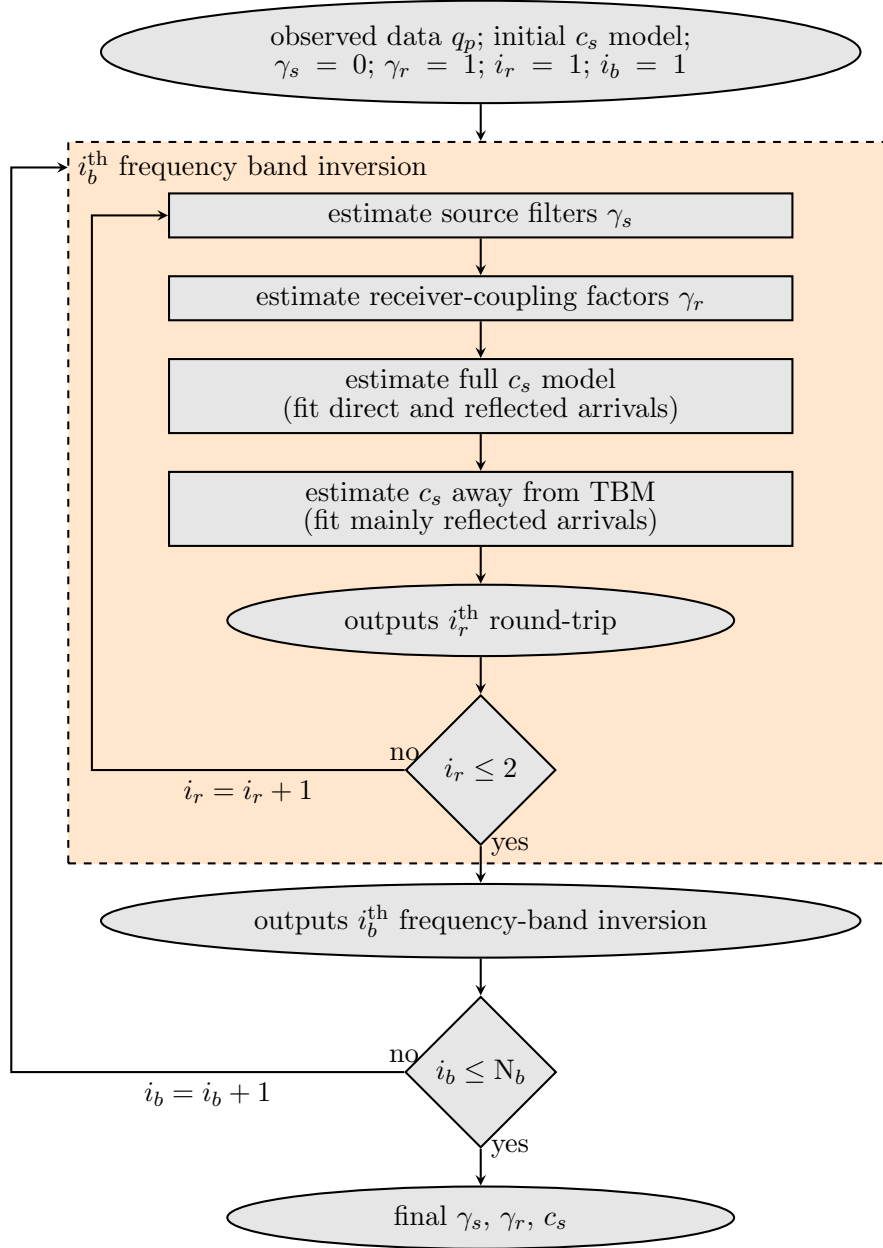


**Figure 2.** Flowchart depicting the optimisation strategy used to estimate source, receivers filters and shear-wave velocity in the medium. The subscript  $b$  in  $i_b$  stands for frequency band and the subscript  $r$  in  $i_r$  stands for round-trip.  $N_b$  denotes the total number of frequency bands inverted.

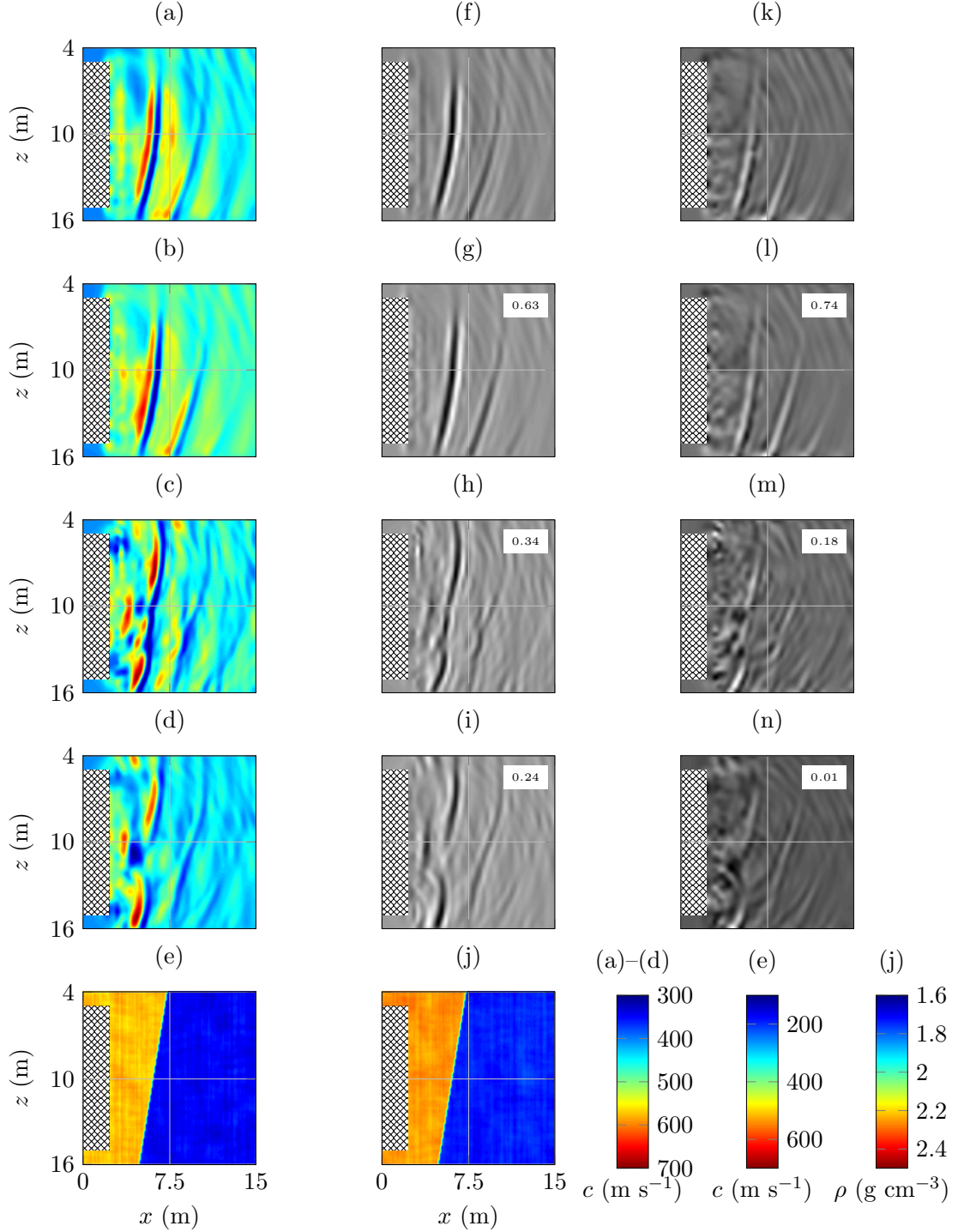


**Figure 3.** Scenario A: Abrupt Change. The output  $c_s$  models using geometries A, B, C and D are plotted in (a), (b), (c) and (d), respectively. The corresponding horizontal and vertical derivatives of the  $c_s$  models are plotted in (f)–(i) and (k)–(n), respectively. The  $c_s$  (e) and  $\rho$  (j) models used to generate the observed data are shown as well. Crosshatch pattern indicates the location of the TBM. The correlation measures of the outputs using geometries B, C and D are also given, where the outputs using geometry A are chosen for reference.

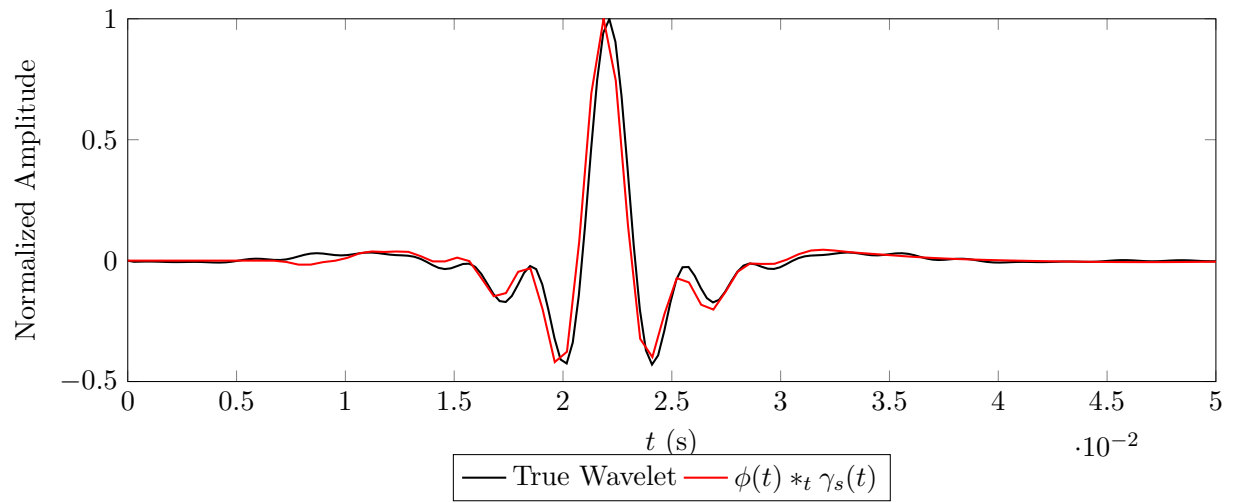


**Figure 4.** For the abrupt-change scenario, the source wavelet used to generate the synthetic *observed* data is plotted in black. The estimated source filter  $\gamma_s$  applied to the modelled-data wavelet  $\phi$  is plotted in red, when using acquisition geometry B.

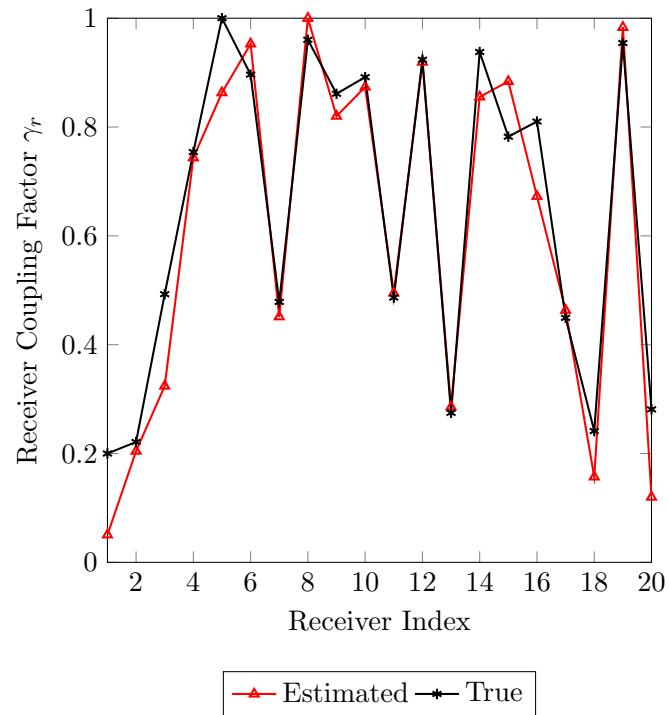


**Figure 5.** For the abrupt-change scenario, the true and estimated receiver-coupling factors are plotted in black and red, respectively. Acquisition geometry B is used.

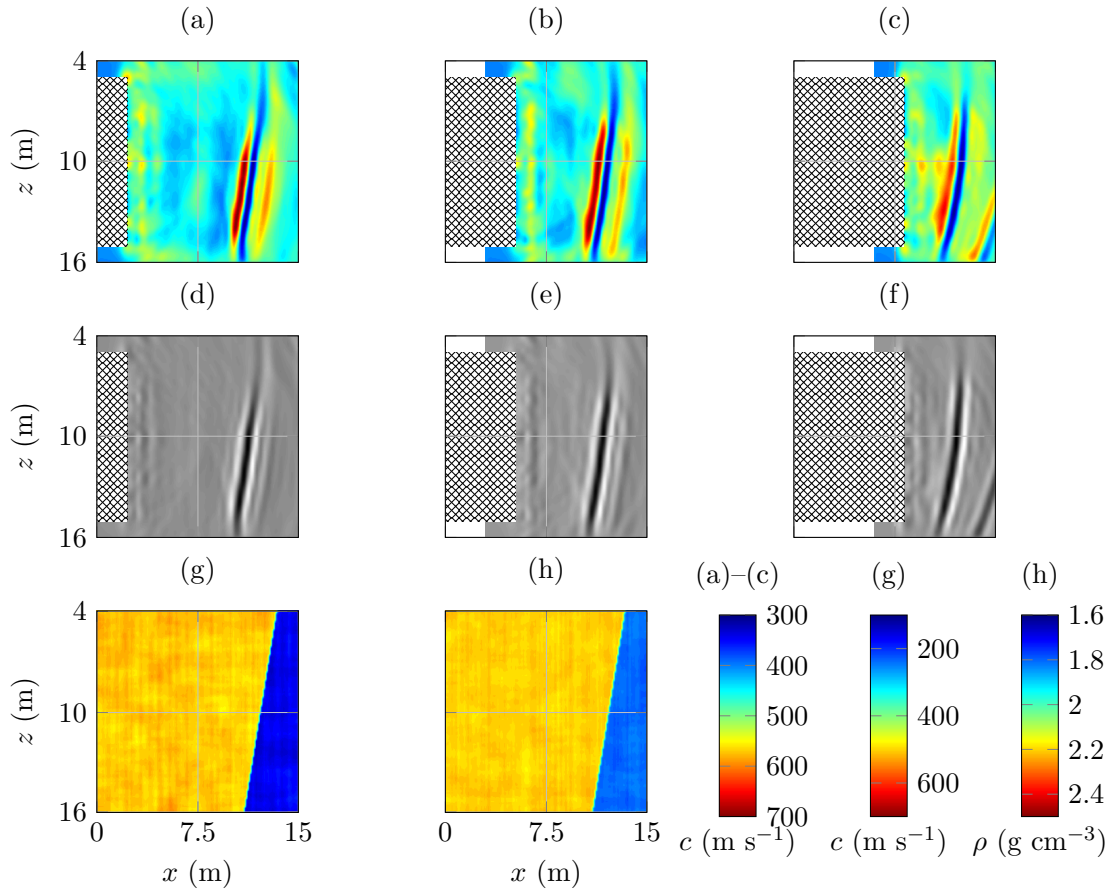


**Figure 6.** Inversion results during three stages of advance of the TBM for Scenario A using acquisition geometry B. The output velocity models from inversion are plotted in (a)–(c). The horizontal derivatives of the output velocity models are plotted in (d)–(f), which depict the target reflector. The cross-hatched pattern indicates the location of the TBM. The  $c_s$  (g) and  $\rho$  (h) models used to generate the observed data are also plotted.

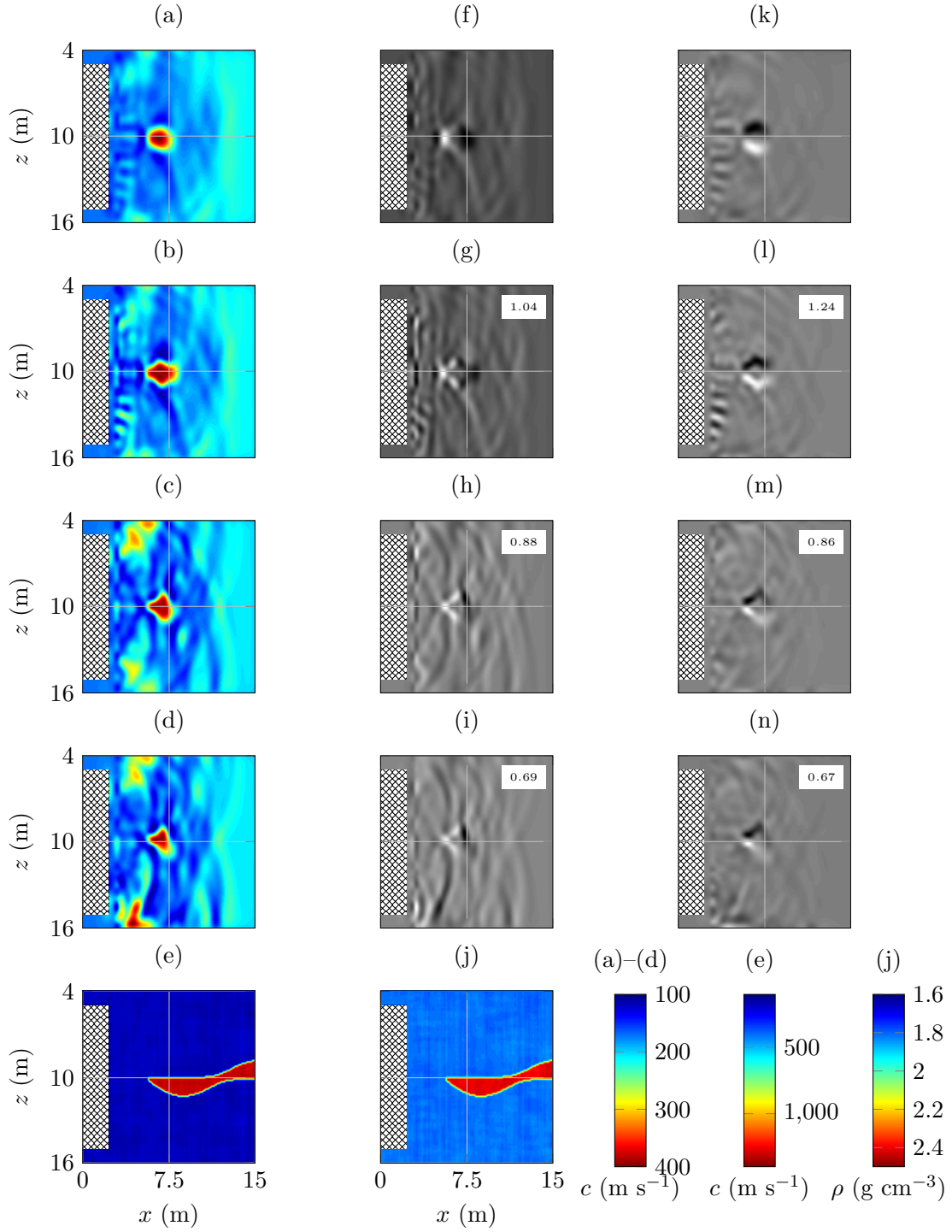
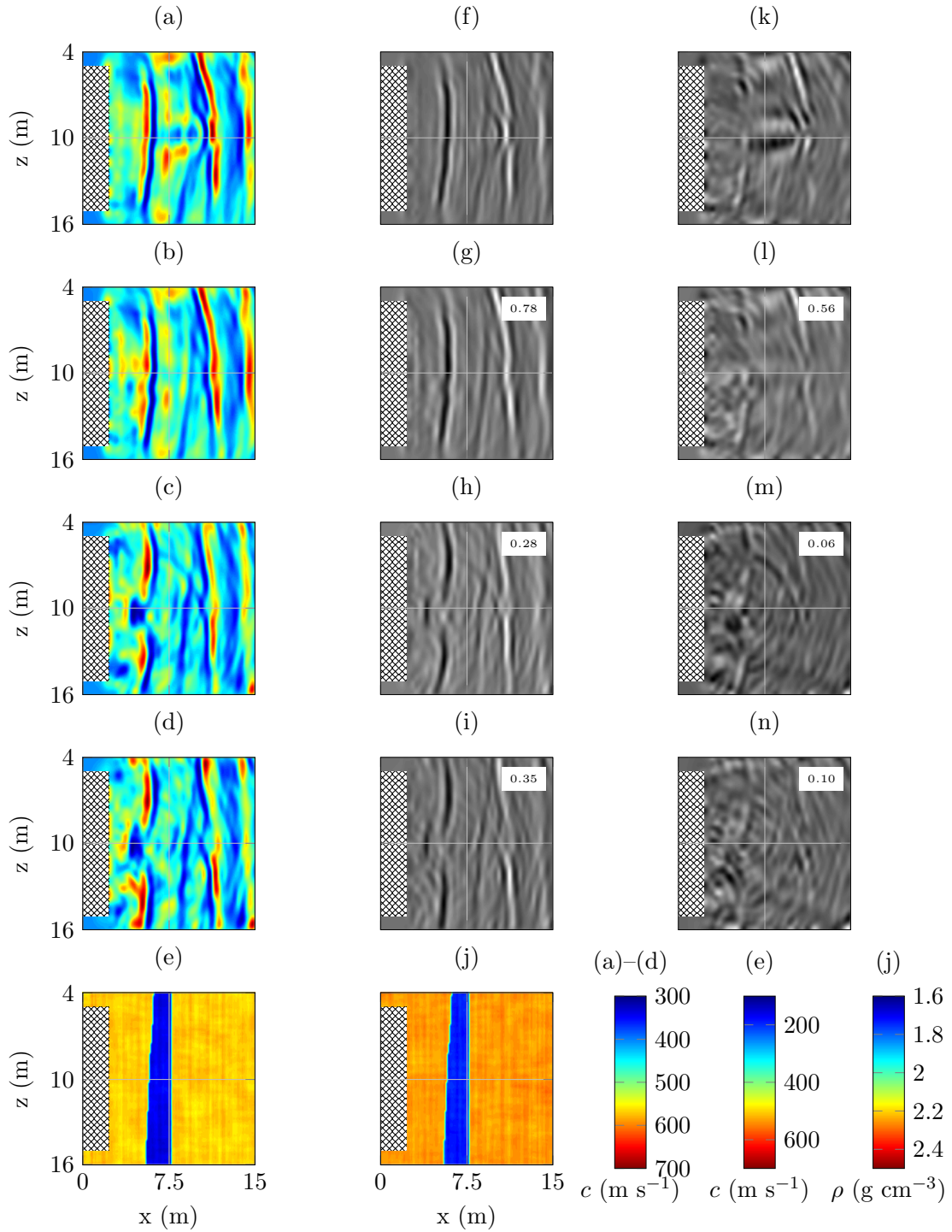


Figure 7. Same as Figure 3, except for Scenario B: Hard-rock Inclusion.





**Figure 8.** Same as Figure 3, except for Scenario C: Fault Region.

Field Experiment in the Netherlands

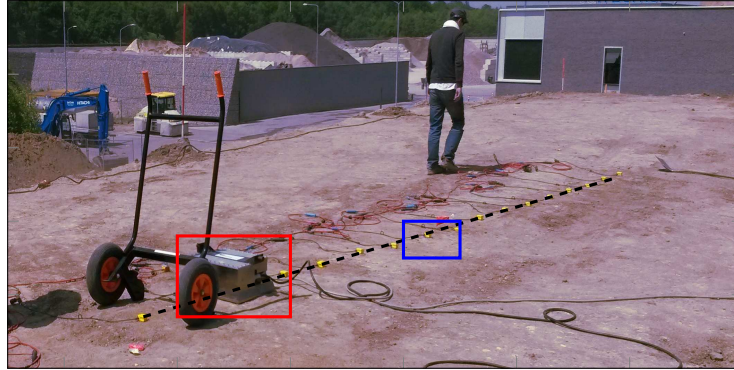


**Figure 9.** Field acquisition with the shear-wave vibrator (marked by the red box), especially designed for this application, and the receivers (blue box) along a transect (dashed line) similar to what is typical for a TBM situation.

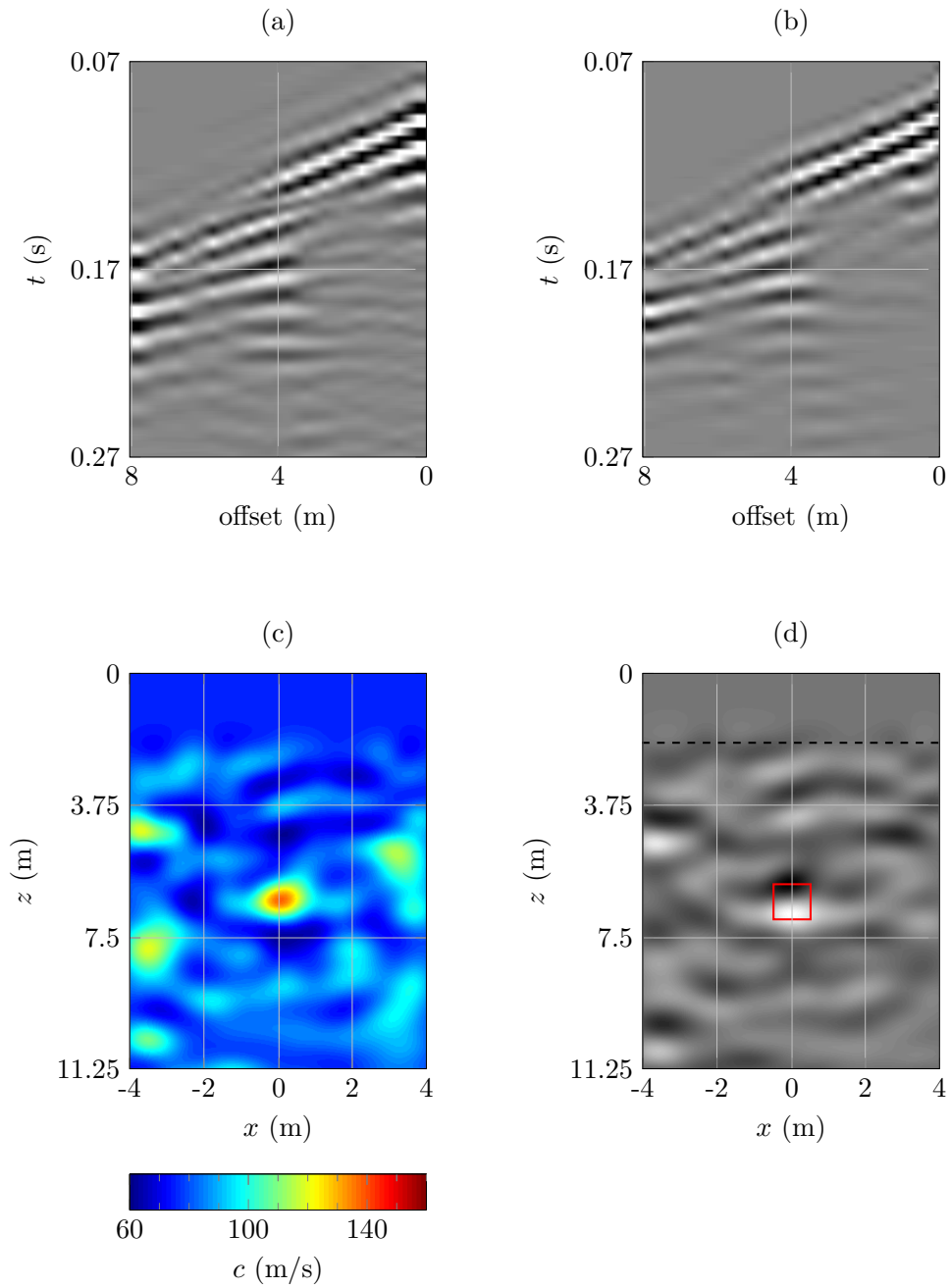


**Figure 10.** The pre-processed data and inversion results of the first transect. a) Observed shot gather for a source at  $x = 4$  m. b) Modelled shot gather after inversion. c) Estimated shear-wave velocity model of subsurface. d) Image of subsurface depicting the inclusion. The actual location of the inclusion is marked by the red box.

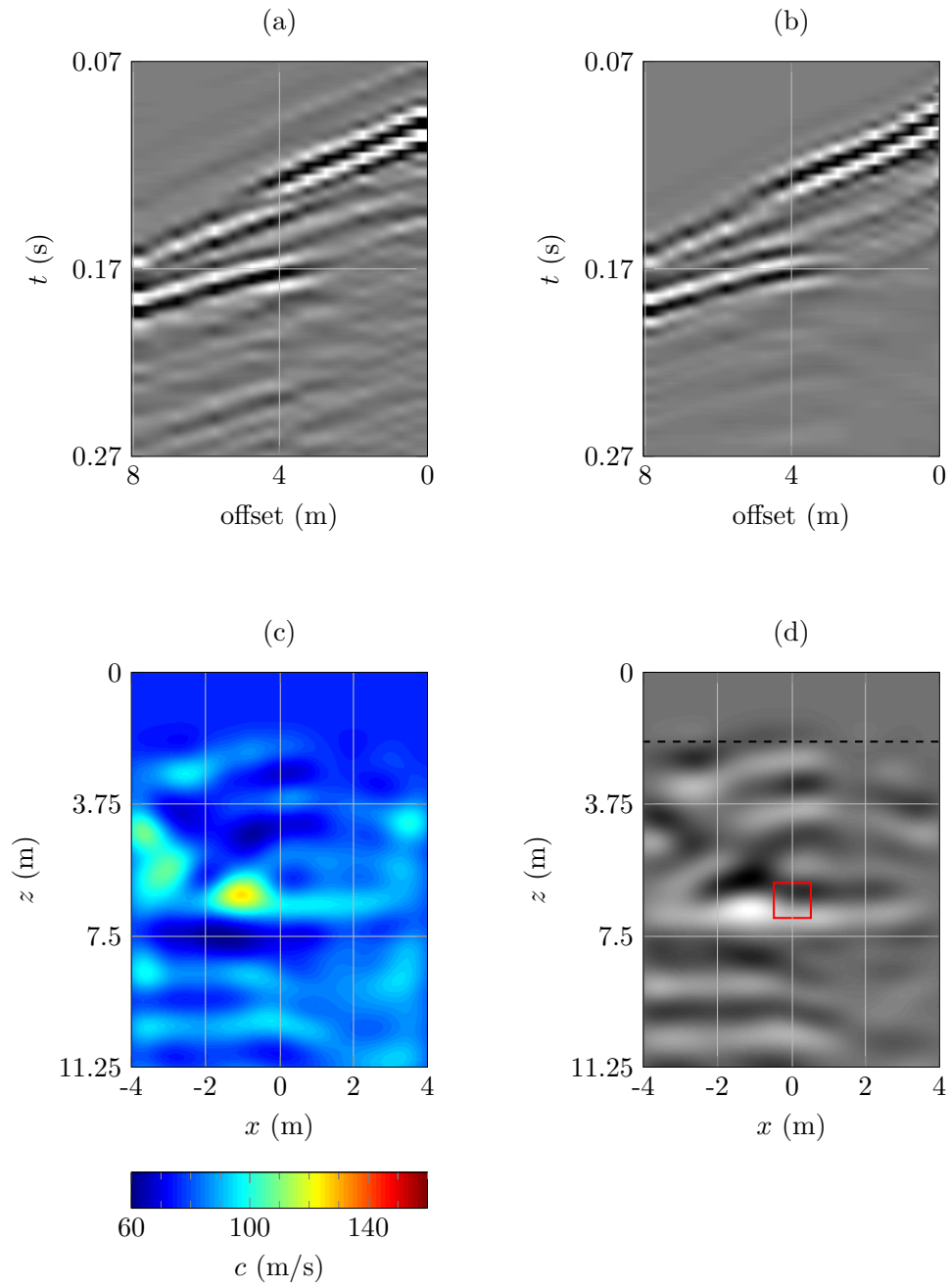


**Figure 11.** Same as Figure 10, except for the data corresponding to the second transect.

**LIST OF TABLES**

- 1 Shear properties of some materials as used in synthetic scenarios, given as shear-wave velocity  $c_s$  and mass density  $\rho$ .
- 2 Forward modelling parameters used for different examples.
- 3 Inversion parameters used in examples.

**Table 1.** Shear properties of some materials as used in synthetic scenarios, given as shear-wave velocity  $c_s$  and mass density  $\rho$ .

Synthetic Scenario(s)		Background Material	Anomaly
Abrupt Change & Fault Region		Sand	Clay
	$c_s$ (m s <sup>-1</sup> )	500	160
	$\rho$ (g cm <sup>-3</sup> )	2.2	1.8
Inclusion		Clay	Limestone
	$c_s$ (m s <sup>-1</sup> )	160	1300
	$\rho$ (g cm <sup>-3</sup> )	1.8	2.4

**Table 2.** Forward modelling parameters used for different examples.

Example	Source wavelet for $q$	Fourth-order minimum-phase Butterworth source wavelet for $p$	Record time (s)
Abrupt Change (synthetic)	40–80–300–400 Hz Ormsby	40–400 Hz	0.1
Inclusion (synthetic)	40 Hz Ricker	1–150 Hz	0.15
Fault Region (synthetic)	40–80–300–400 Hz Ormsby	40–400 Hz	0.1
Inclusion (field)	unknown	10–120 Hz	0.35

**Table 3.** Inversion parameters used in examples.

Scenario	Band 1 (Hz)	Band 2 (Hz)	Band 3 (Hz)	Band 4 (Hz)	Length of $\gamma_s$ (s)	Initial $c_s$ (m s <sup>-1</sup> )
Abrupt change (synthetic)	40–70	40–100	40–200	40–400	0.01	400
Inclusion (synthetic)	full				0.01	170
Fault Region (synthetic)	40–70	40–100	40–200	40–400	0.01	400
Inclusion (field)	full				0.04	110